Chapter 10

Application of Phase-Field Method to the Analysis of Phase Decomposition of Alloys

Erika O. Avila-Davila, Victor M. Lopez-Hirata and Maribel L. Saucedo-Muñoz

Additional information is available at the end of the chapter

http://dx.doi.org/10.5772/64153

Abstract

This chapter is focused on the application of the phase-field method to the analysis of phase decomposition during the isothermal aging of alloys. The phase-field method is based on a numerical solution of either the nonlinear Cahn-Hilliard equation or the Cahn-Allen equation. These partial differential equations can be solved using the finite difference method among other numerical methods. The phase-field method has been applied to analyze different types of phase transformations in alloys, such as phase decomposition, precipitation, recrystallization, grain growth, solidification of pure metals and alloys, martensitic transformation, ordering reactions, and so on. One of the main advantages of phase-field method is that this method permits to follow the microstructure evolution in two or three dimensions as the time of phase transformations progresses. Thus, the morphology, size, and size distribution could be determined to follow their corresponding growth kinetics. Additionally, the evolution of chemical composition can also be followed during the phase transformations. Furthermore, both Allen-Cahn and Cahn-Hilliard equations can be solved simultaneously to analyze the presence of ordered phases or magnetic domains in alloys.

The formation of phases in alloys usually takes place by nucleation mechanism, growth mechanism, or spinodal decomposition mechanism, which is followed by the coarsening of phases in alloy systems. These three processes can be been analyzed using the phase-field method and their results can also be compared with the fundamental theories of phase transformations such as the Cahn-Hilliard spinodal decomposition theory and the Lifshitz-Slyozov-Wagner diffusion-controlled coarsening theory.

Therefore, this chapter first deals with the analysis of phase decomposition during the isothermal aging of hypothetical binary alloys using the nonlinear Cahn-Hilliard equation. To continue, the effect of main parameters, such as the atomic mobility interface energy and alloy composition, on the microstructure evolution and growth kinetics are discussed. To conclude, the application of phase-field method is extended

to the analysis of phase decomposition during isothermal aging of real binary and ternary alloy systems, such as Fe-Cr, Cu-Ni, and Cu-Ni-Fe. A comparison of simulated results with experimental ones is also included.

Keywords: phase field method, phase decomposition, alloys, aging

1. Introduction

In the field of materials science, it is important to analyze different moving free boundary problems in order to understand its effect on the phase transformations that may occur in materials. For instance, the solidification and grain growth, and martensitic transformation are diffusion-controlled and diffusion-less phase transformations, respectively, with this characteristic. One way to overcome this need is the use of the diffuse interface model [1]. Furthermore, the application of the phase-field method to this sort of problem permits the use of the order parameter and phase-field variable which takes into account the composition gradient energy present in a diffuse interface model. For instance [2], the order parameter φ could takes values either 0 or 1, which may represent the liquid or solid states, respectively, during the solidification process of a pure metal.

The phase-field method is based on the equations proposed by Cahn-Hilliard [1], Allen-Cahn [2], or Ginzburg-Landau [3]:

$$\frac{\partial c_i(x,t)}{\partial t} = \nabla.\left(\sum_j M_{ij} \nabla \frac{\partial G_{sys}}{\partial c_i(x,t)} \right) \tag{1}$$

$$\frac{\partial \phi_i(x,t)}{\partial t} = -\sum_j L_{ij} \left(\frac{\partial G_{sys}}{\partial \phi_i(x,t)} \right) \tag{2}$$

where $c_i(x,t)$ and $\varphi_\iota(x,t)$ correspond to the field variable, for instance, concentration and order parameter as a function of position x and time t. M_{ij} and L_{ij} are the mobility. The free energy of a given system may include, for instance, the following terms [4]:

$$G_{sys} = F_c + F_{grad} + F_{str} + F_{mag} + F_{ele} \tag{3}$$

F_c is the local free energy, F_{grad} the compositional gradient energy, F_{str} the elastic strain energy, and F_{mag} and F_{ele} the energies corresponding to magnetic and electric effects, respectively.

The composition gradient energy can be defined, for instance, for the field variable, concentration c, by the following mathematical expression [1]:

http://dx.doi.org/10.5772/64153

$$F_{grad} = \frac{1}{2}\int_r k(\nabla c)^2 dr \tag{4}$$

where κ is the gradient energy coefficient.

One of the main advantages of phase-field method is that this method permits to follow the microstructure evolution in two or three dimensions as the time of phase transformations progresses. Thus, the morphology, size, and size distribution could be determined to follow their corresponding growth kinetics. Additionally, the evolution of chemical composition can also be followed during the phase transformations.

To solve either of the partial differential equations, Eqs (1) or (2), several numerical methods have been used such as finite difference method, difference volume method, and finite element method [5]. The use of explicit finite difference method is simple and good alternative to solve this type of differential equations. For instance, the finite difference method can be used to solve a simple partial differential equation such as the simplified one-dimension equation of the second Fick's law:

$$\frac{\partial c}{\partial t} = D\frac{\partial^z c}{\partial x^2} \tag{5}$$

where D is the diffusion coefficient. The finite difference solution can be approximated as follows [6]:

$$\frac{c_i^{t+1} - c_i^t}{\Delta t} = D\frac{c_{i+1}^t - 2c_i^t + c_{i-1}^t}{\Delta x^2} \tag{6}$$

where t indicates the time and $t + 1$ is equal to $t + \Delta t$ being Δt the time step. The spacing between two nodes is Δx, the distance step. The node number corresponds to i. c_i^{t+1} indicates the calculated concentration for the node i in the next time step, $t + \Delta t$ and c_i^t that of the previous time t.

This chapter is mainly focused on the application to the phase decomposition by the spinodal decomposition mechanism during the isothermal aging of hypothetical binary alloys using the nonlinear Cahn-Hilliard equation [7]. The effect of main parameters such as the atomic mobility of alloy and elastic-strain energy on the microstructure evolution and growth kinetics is analyzed. To conclude, the application of phase-field method is extended to the analysis of spinodal decomposition during isothermal aging of real binary and ternary alloy systems, such as Cu-Ni, Fe-Cr, and Cu-Ni-Fe. A comparison of simulated results with experimental ones is also included.

2. Phase decomposition in alloys

The formation of phases in alloys usually takes place by nucleation mechanism, growth mechanism, or spinodal decomposition mechanism, which is followed by the coarsening of phases in alloy systems. These three processes can be analyzed using the phase-field method, and their results can also be compared with the fundamental theories of phase transformations such as the Cahn-Hilliard spinodal decomposition theory [4] and the Lifshitz-Slyozov-Wagner (LSW) diffusion-controlled coarsening theory [8]. The phase decomposition that takes place by the spinodal decomposition mechanism is distinguished from the phase separation that occurs by nucleation and growth mechanism by the formation of an initial composition modulation, which shows an increase in the modulation amplitude with time. In contrast, the phase formation by nucleation and growth predicts that the formed phase has a composition very close to the equilibrium one from the start to the finish of phase transformation [9]. Besides, the spinodal decomposition is usually associated with the presence of a miscibility gap in the equilibrium phase diagram, as shown in **Figure 1**. The miscibility gap is the equilibrium line and there is only one α phase for compositions and temperatures above this line, whereas a mixture of two phases, α_1 and α_2, is present inside the miscibility gap. This figure also shows the existence of the chemical spinodal located within the miscibility gap. A supersaturated α_{sss} phase is expected to decompose spinodally into a mixture of A-rich α_1 and B-rich α_2 phases for an alloy composition after heating at a temperature higher than that of the miscibility gap and then quenching and heating or aging at a temperature lower than the chemical spinodal. The miscibility gap in **Figure 1** is usually related to the plot of free energy versus composition shown in **Figure 2**. This figure shows the free energy curve shape changes as the temperature decreases. This type of curve is known as the spinodal curve, and it indicates that any alloy composition is in unstable state and thus it is expected to decompose into a mixture of A-rich α_1 and B-rich α_2 phases. The minimum and saddle points at each temperature of the spinodal curve correspond to the equilibrium and chemical spinodal shown in **Figure 1**.

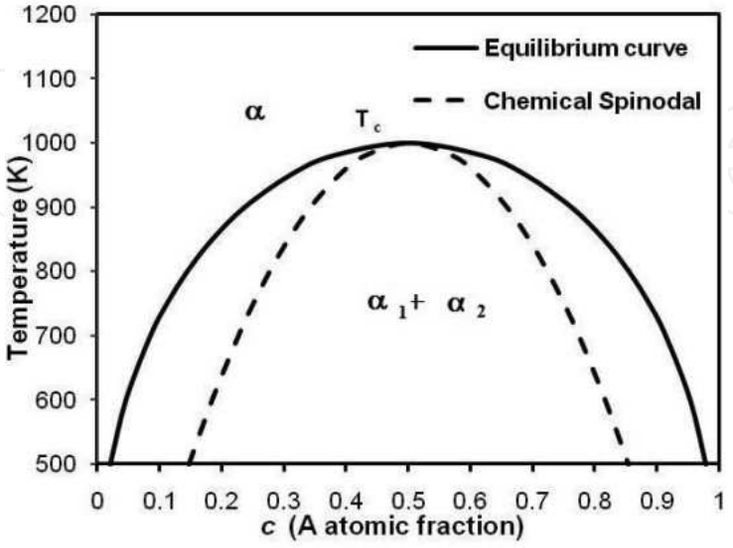

Figure 1. Miscibility gap in a hypothetic A-B phase diagram.

http://dx.doi.org/10.5772/64153

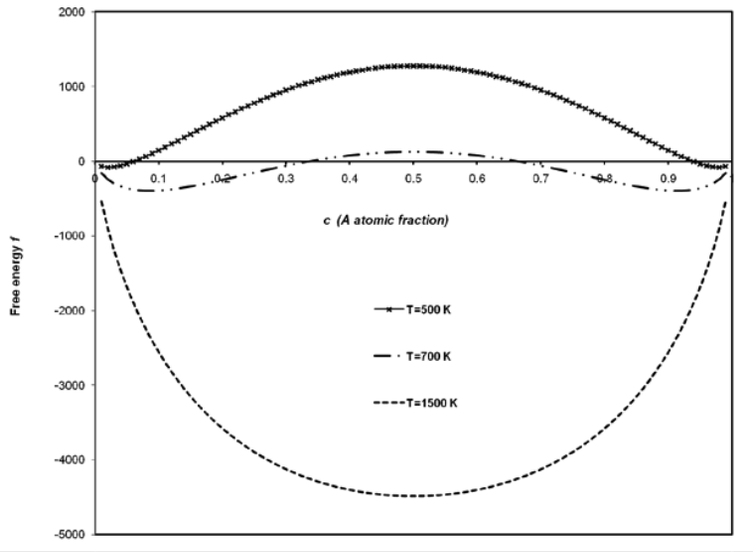

Figure 2. Plot of free energy versus composition for the miscibility gap in **Figure 1**.

The Cahn-Hilliard theory of spinodal decomposition [4] was developed by the modification of the second Fick's law equation in order to allow only the growth of the modulation amplitude in composition with a wavelength larger than a critical value. Furthermore, the nonlinear Cahn-Hilliard equation, used in the simulations of this work, has its origin in this theory.

3. Simulation of hypothetic binary alloys

In the numerical simulation of the phase decomposition for a hypothetic A-B binary alloy, the nonlinear Cahn-Hilliard equation [7] can be rewritten as follows:

$$\frac{\partial c_i(x,t)}{\partial t} = M_i \nabla^2 \left(\frac{\partial f_o(c)}{\partial c_i} - K_i \nabla^2 c_i \right) \tag{7}$$

The local chemical free energy $f_o(c)$ was assumed to follow the following equation [10]:

$$f_0 = -(c - 0.5)^2 + 2.5(c - 0.5)^4 \tag{8}$$

This equation represents a spinodal curve similar to those shown in **Figure 2**. In the first case of simulation, the mobility M_i was considered to be constant and equal to 1, and the composition c is equal to 0.4. The calculated concentration profiles for different times are shown in **Figure 3**. The initial modulation amplitude increases with time which confirms that the phase decomposition occurs by the spinodal decomposition mechanism [4]. Besides, the initial composition modulation forms a mixture of A-rich α_1 and B-rich α_2 phases as a result of heating

at a temperature with mobility M_i equal to 1. An advantage of the phase-field method is that the microstructure evolution can be obtained by plotting the concentration in two dimensions. **Figure 4** shows the calculated microstructures as a function of time. The black and white zones correspond to the A-rich α_1 and B-rich α_2 phases, respectively. The morphology of the decomposed phases is irregular and interconnected as predicted by the Cahn-Hilliard theory of spinodal decomposition [4]. The coarsening process of the decomposed phases is also observed for the longer times.

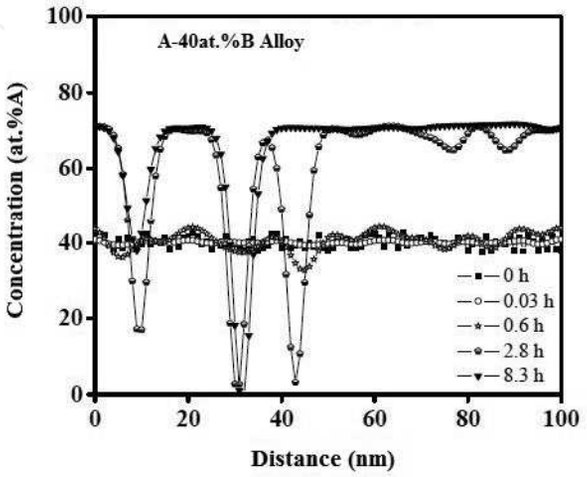

Figure 3. Concentration profiles for the numerical simulation of $M_i = 1$ and $c = 0.4$.

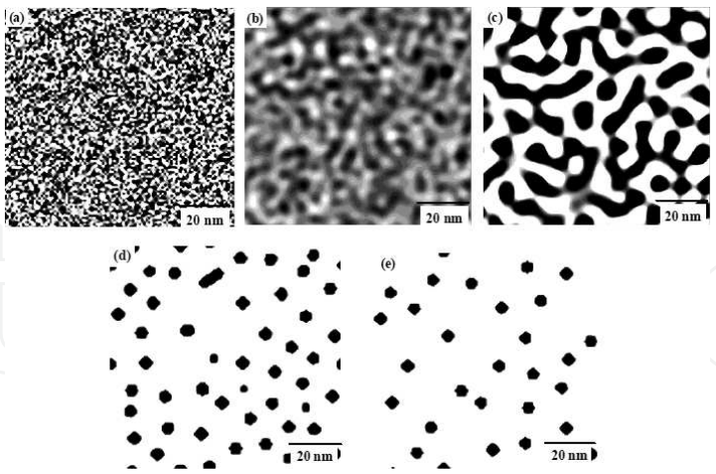

Figure 4. Microstructure evolution for $M_i = 1$ and $c = 0.4$ for (a) 0 h, (b) 0.03 h, (c) 0.6 h, (d)2.8 h, and (e) 6.3 h.

In the second example, the mobility M_i was not constant and defined with the following equation:

$$M_i = 1 - \alpha c^2 \tag{9}$$

http://dx.doi.org/10.5772/64153

where $\alpha = 1$ and the nonlinear Cahn-Hilliar equation was modified as follows:

$$\frac{\partial c_i(x,t)}{\partial t} = \nabla\left[M_i \nabla\left(\frac{\partial f_0(c)}{\partial c_i} - K_i \nabla^2 c_i \right) \right] \tag{10}$$

The numerical solution of the former partial differential equation conducted to the following concentration profiles (**Figure 5**). The same characteristics described in the previous example are also observed for this case. However, the amplitude of the composition modulation for this case increases faster with time than that for the former case. The microstructure evolution for this case is different from the one shown for the previous case (**Figure 6**). That is, the decomposed phases form a lamellar structure instead of the irregular and interconnected morphology of the previous case. This may be attributed to the variable mobility of the decomposed phases [4].

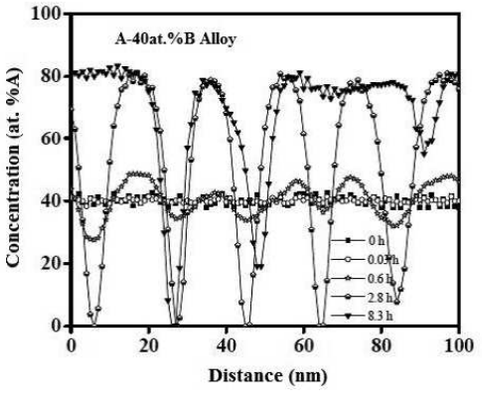

Figure 5. Concentration profiles for the numerical simulation of variable M_i and $c = 0.4$.

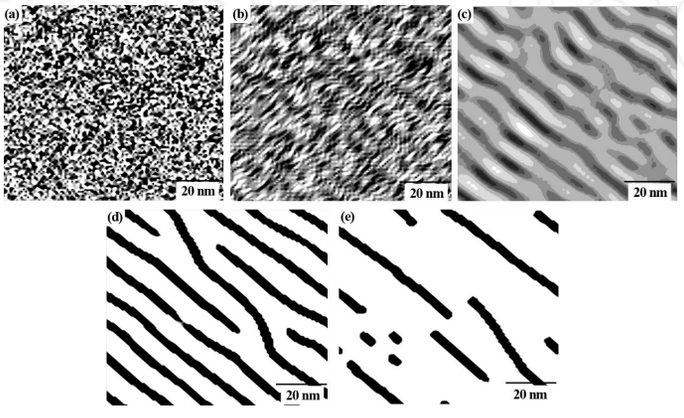

Figure 6. Microstructure evolution for variable M_i and c= 0.4 for (a) 0 h, (b) 0.03 h, (c) 0.6 h, (d)2.8 h, and (e) 6.3 h.

To complete the numerical simulation of hypothetic binary alloys, the next case includes the presence of an isotropic elastic-strain energy f_{el} with a value equal to 1 and M_i equal to 1. The nonlinear Cahn-Hilliard equation was modified as follows:

$$\frac{\partial c_i(x,t)}{\partial t} = M_i \nabla^2 \left(\frac{\partial f_o(c)}{\partial c_i} + \frac{\partial f_{el}}{\partial c_i} - K_i \nabla^2 c_i \right) \tag{11}$$

Figure 7 illustrates the concentration profiles for this case and the same characteristics, observed in the others, are also present. That is, the modulation amplitude increases with time. Besides, a mixture of A-rich α_1 and B-rich α_2 phases is formed after aging. The microstructure evolution is similar to that of the first case for short times. That is, the morphology of the decomposed phases is irregular and interconnected, which is known as percolated structure [4] (**Figure 8**). Nevertheless, one of the decomposed phases takes a cuboid shape for the longest times, which is attributed to the isotropic elastic-stain energy [9].

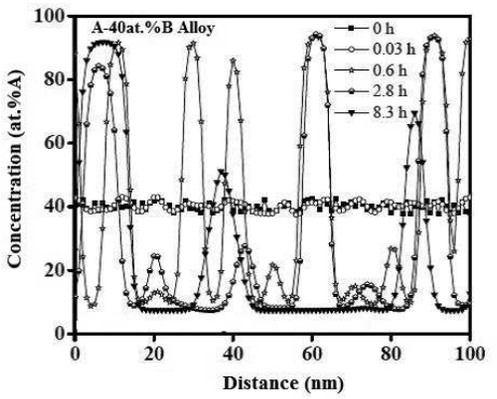

Figure 7. Concentration profiles for the numerical simulation of f_{el} = 1 and c = 0.4.

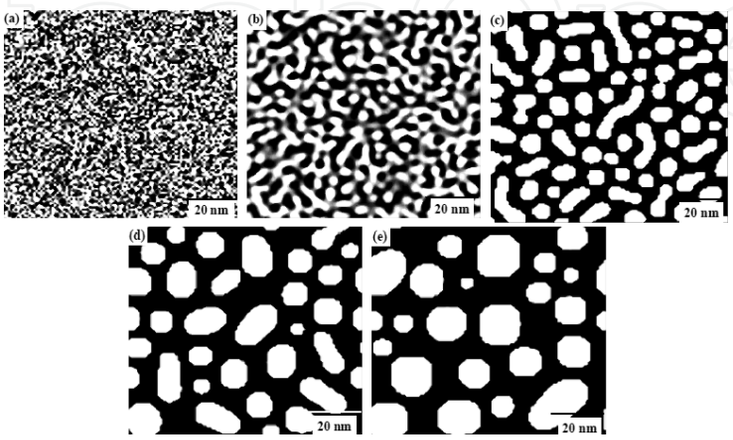

Figure 8. Microstructure evolution for f_{el} = 1 and c = 0.4 for (a) 0 h, (b) 0.03, (c) 0.6 h, (d)2.8 h, and (e) 6.3 h.

http://dx.doi.org/10.5772/64153

4. Simulation in real binary alloys

In the next part of this chapter, the numerical simulation of the phased decompositions of Cu-Ni and Fe-Cr alloys after aging at different temperatures for different times is shown. Simulated results are compared to the experimental ones. To begin, the Cu-Ni alloys are widely used in different industrial applications. The equilibrium phase diagram is shown in **Figure 9**. This diagram has a miscibility gap located at temperatures lower than 350°C [11]. Thus, a supersaturated solid solution, formed by heating above 350°C and then quenching, is expected to decompose spinodally into a mixture of Cu-rich and Ni-rich phases after aging at a temperature lower than 350°C. Nevertheless, the growth kinetics of spinodal decomposition is very slow due to the low atomic diffusivity at these temperatures [7]. Thus, the application of the phase-field method to analyze the spinodal decomposition seems to be a good alternative because of the slow kinetics.

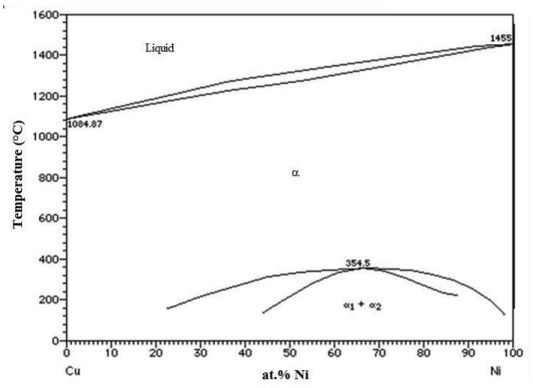

Figure 9. Equilibrium Cu-Ni phase diagram [11].

The nonlinear Cahn-Hilliard equation, Eq. (7), was solved to analyze the phase decomposition in these alloys. The local energy f_o was defined using the regular solution model as follows [7]:

$$f_o = f_{Cu}\, c_{Cu} + f_{Ni}\, c_{Ni} + \Omega_{Cu-Ni}\, c_{Cu}\, c_{Ni} + RT\,(c_{Cu}\,\ln c_{Cu} + c_{Ni}\ln c_{Ni}) \tag{12}$$

where R is the gas constant, T is the absolute temperature. f_{Cu} and f_{Ni} are the molar free energy of pure Cu and Ni, respectively, and $\Omega_{Cu\text{-}Ni}$ is the interaction parameter. The atomic mobility M_i is related to the interdiffusion coefficient $\bar{D}_{\mathrm{i}}$ as follows:

$$\overline{D}_i = M_i\left(\frac{\partial^2 f_o}{\partial c_i^{\,2}}\right) \tag{13}$$

The interdiffusion coefficient $\bar{D}_i$ was assumed to be defined as follows [4]:

$$\overline{D}_i = D_{Ni} c_{Cu} + (1 - c_{Cu}) D_{Cu} \tag{14}$$

The gradient energy coefficient K was determined as proposed by reference [4]:

$$K = \left(\frac{2}{3}\right) h_{0.5}^{M} r_0^2 \tag{15}$$

where $h_{0.5}^{M}$ is the mixing heat per unit volume at $c = 0.5$ and r_o is the nearest neighbor distance. The heat of mixing h^M was determined according to the next equation [4]:

$$h^M = c_{Cu}\, c_{Ni}\, \Omega_{Cu-Ni} \tag{16}$$

The thermodynamic, diffusion, crystal lattice, and elastic parameters for the microstructure simulation were obtained from the literature [12–15] and these are shown in **Table 1**. The effect of coherency elastic-strain energy was considered to be present during the phase decomposition of Cu-Ni alloys in spite of the similar lattice parameters of copper and nickel [13]. This elastic-strain energy was introduced into Eq. (7), according to the simple definition proposed by Hilliard [4]:

Parameter	Ni-Cu alloys	
Crystal lattice parameter a(nm) [13]	0.360	
η (nm) [13]	0.0016	
$\Omega_{Cu\text{-}Ni}$ (J mol^{-1}) [12]	(8366.0 + 2.802T) + (−4359.6 + 1.812T)(c_{Cu}-c_{Ni})	
Diffusion coefficient D (cm^2 s^{-1}) [14]	Cu 1.5–2.3 exp (−230,000–260,000 J mol^{-1})/RT	
	Ni 17–35 exp (−270,000–300,000 J mol^{-1})/RT	
c_{ij} (J m^{-3})	c_{11} = 16.84 × 10^{10}	c_{11} = 24.65 × 10^{10}
Cu/Ni [15]	c_{12} = 12.14 × 10^{10}	c_{44}= 12.47 × 10^{10}
	c_{44} = 7.54 × 10^{10}	

Table 1. Values of lattice, diffusion, thermodynamic and elastic constants.

$$f_{el} = A \int \eta^2\, Y\, (c - c_0)^2\, dx \tag{17}$$

where A is the cross-sectional area and Y is an elastic constant defined by the elastic stiffness constants, c_{11}, c_{12}, and c_{44}, for the Cu-rich and Ni-rich phases. The parameter η is equal to d$\ln a$/dc. In the case of fcc metals, the elastic energy will be a minimum for the <100> crystallographic directions, and thus the Y value can be assumed similar to that corresponding to an isotropic material [4]:

http://dx.doi.org/10.5772/64153

$$Y_{<100>} = c_{11} + c_{12} - 2\left(\frac{c_{12}^2}{c_{11}}\right) \tag{18}$$

The elastic constants, c_{ij}, were calculated as follows:

$$c_{ij} = c_{ij}^{Cu} c_{Cu} + c_{ij}^{Ni}(1 - c_{Cu}) \tag{19}$$

Considering the elastic strain energy, f_{el}, Eq. (7) was rewritten as Eq. (11).

The microstructural simulation was carried out using the finite difference method with 101 × 101 points square grid with a mesh size of 0.25 nm and a time-step size of 10 s. The simulations were performed for the Ni-30at.% Cu alloy at temperatures between 250 and 322°C for different times.

Figure 10 shows the numerically calculated plots of Cu concentration versus distance for the Ni-30at.%Cu alloy solution treated (0 h) and aged at 300°C for different times. There is an increase in the modulation amplitude with aging time. The increase in amplitude at this temperature confirms that the phase decomposition occurs spinodally in this alloy. The long simulated aging times also confirm that the growth kinetics of phase decomposition is very slow in this alloy system.

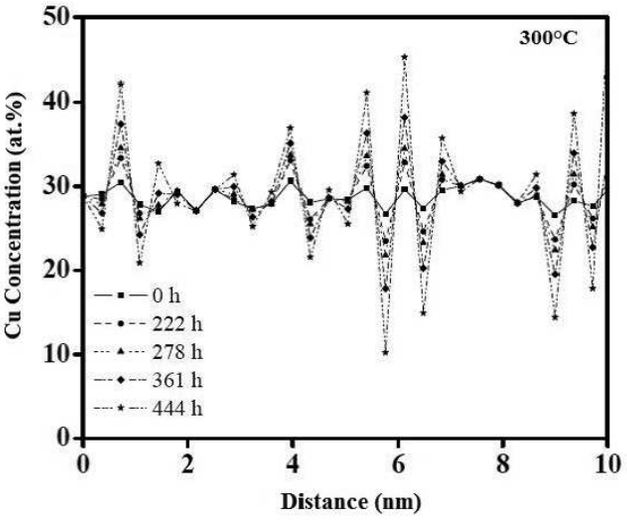

Figure 10. Ni-30at.%Cu alloy aged at 300°C.

The simulated microstructures of the Ni-30at.%Cu alloy aged at 300°C for 0, 222, 278, 361, and 444 h are shown in **Figure 11 (a–e)**, respectively. The black and white regions correspond to the Cu-rich and Ni-rich phases, respectively. It can be seen that the morphology of the decomposed phases is irregular and interconnected. The volume fraction of the Ni-rich phase increased with aging time.

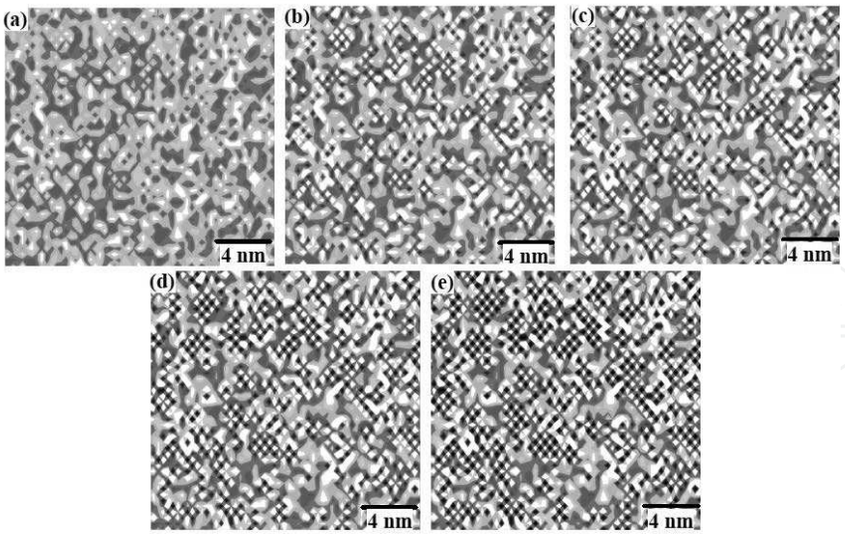

Figure 11. Microstructure evolution of Ni-30at.%Cu alloy aged at 300°C for (a) 0 h, (b) 222 h, (c) 278 h, (d) 361 h, and (e) 444 h.

The experimental Ne-gas field ion microscopy (FIM) images of the Ni-30at.%Cu alloy aged at 300°C for 500 h is shown in **Figure 12**. There is a good agreement between the calculated and experimental morphologies of the decomposed phases.

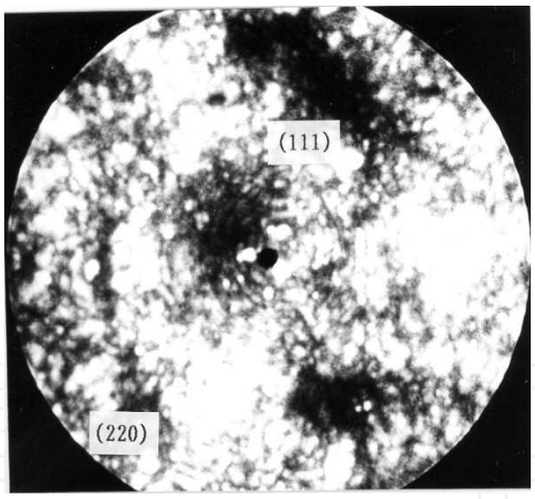

Figure 12. Ne FIM image of the Ni-30at.%Cu alloy aged at 300°C for 500 h.

In the next paragraphs, a second example about the numerical simulation of real alloys is presented. The Fe-Cr alloys are a very important alloy system since this is used as the basis for different industrial alloys, such as the family of stainless steels. The Fe-Cr equilibrium phase diagram [11] also shows a miscibility gap found at temperatures lower than 500°C (**Figure 13**). Thus, the phase decomposition of the supersaturated solid solution into a mixture of Cr-rich and Fe-rich phases is also expected as a result of aging at temperatures lower than 500 °C.

http://dx.doi.org/10.5772/64153

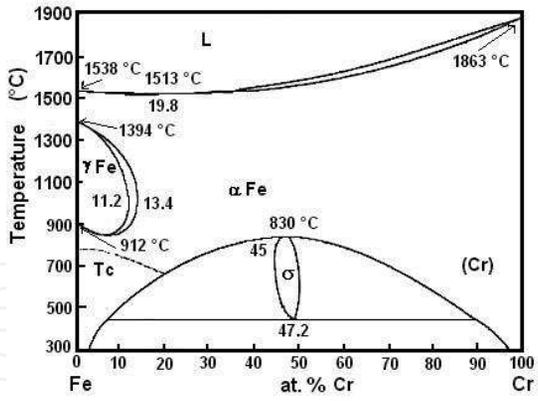

Figure 13. Equilibrium Fe-Cr phase diagram [11].

The phase decomposition simulation was based on a numerical solution of the nonlinear Cahn-Hilliard equation, Eq. (7). The formulation for this case is very similar to that described previously for the numerical simulation of the phase decomposition in Ni-Cu alloys.

The crystal lattice, thermodynamic, diffusion, and elastic constants for the microstructural simulation in Fe-Cr alloys were taken from references [13–16] and these parameters are shown in **Table 2**. The simulation of phase decomposition was pursued using the explicit finite difference method with 101 × 101 and 201 × 201 points square grids with a mesh size of 0.1 and 0.25 nm and a time-step size up to 10 s. The numerical simulation was performed for the Fe-40at.%Cr alloy aged at 470°C for times from 0 to 1000 h. It is important to mention that the initial composition modulation corresponding to the solution-treated sample was calculated using a random number generator.

Parameter	Values
Crystal lattice parameter a (nm) [13]	0.2866
η(nm) [13]	0.00614
$\Omega_{Fe\text{-}Cr}$ (J mol^{-1}) [16]	(18600.0 + 0.1T)
Diffusion coefficient D (cm^2 s^{-1}) [16]	D_{Fe} = 1.2 exp (−294,000 J mol^{-1})/RT
	D_{Cr} = 0.2 exp (−308,000 J mol^{-1})/RT
c_{ij} (J m^{-3}) [15]	
Fe	c_{11}= 23.10 × 10^{10} c_{12} = 13.54 × 10^{10} c_{44} = 11.78 × 10^{10}
Cr	c_{11} = 35.00 × 1010 c_{12} = 67.80 × 10^{10} c_{44} = 10.08 × 10^{10}

Table 2. Lattice, diffusion, elastic, and thermodynamic parameters.

The plots of Cr concentration versus distance, concentration profiles, for the Fe-40at.%Cr alloy aged at 470°C for different times are shown in **Figure 14**. These concentration profiles indicate clearly that the supersaturated solid solution decomposed spinodally into a mix of Cr-rich and Fe-rich phases since the modulation amplitude increases as the aging time increases.

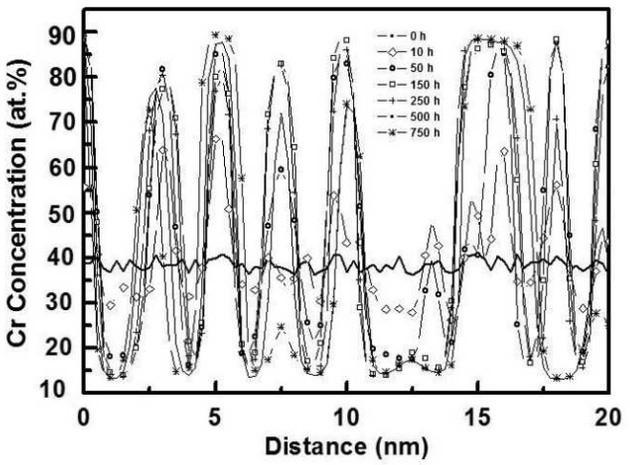

Figure 14. Concentration profiles of Fe-40at.%Cr alloy aged at 470°C.

Figure 15 shows the simulated microstructural evolution of the phase decomposition in the Fe-40-at.%Cr alloy aged at 470°C for times from 10 to 750 h. The white and gray zones represent the Fe-rich and Cr-rich phases, respectively. It can be observed and irregular and interconnected morphology of the decomposed phases in the alloy aged for times up to 10 h. This morphological characteristic is known as percolated structure, and it has been commonly observed to occur during the early stages of aging in the spinodally decomposed alloys. The HR-TEM micrographs of this alloy aged at 470°C for 250 h shows clearly the presence of spheres corresponding to the Cr-rich phases imbedded in the ferrite phase matrix (**Figure 16**). The decomposed phases present a coherent interface. This shape of decomposed Cr-rich phase is in good agreement with the simulated microstructure (**Figure 15(e)** and **(f)**) [17].

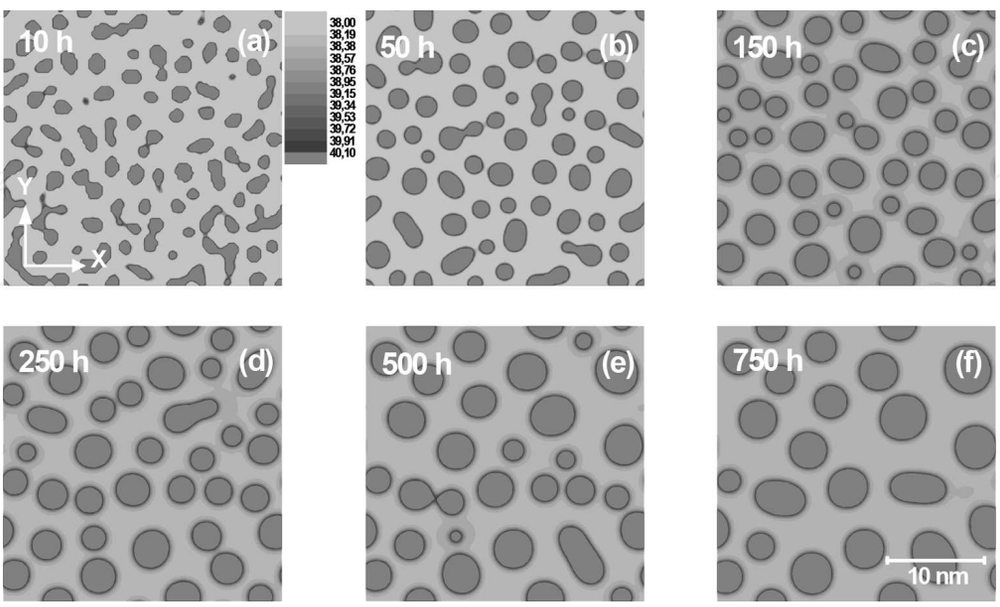

Figure 15. Microstructure evolution of Fe-40at.%Cr alloy aged at 470°C.

http://dx.doi.org/10.5772/64153

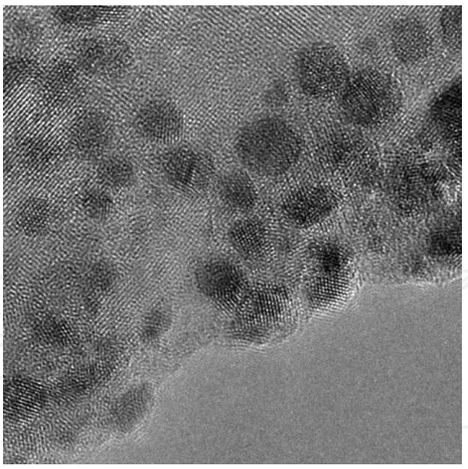

Figure 16. HR-TEM micrograph of Fe-40at.%Cr alloy aged at 470°C for 250 h.

5. Simulation in real ternary alloys

The numerical simulation of phase decomposition of ternary alloys can be also conducted using the phase-field method. The equilibrium Cu-Ni-Fe phase diagram [18] is shown in **Figure 17** at different temperatures. The presence of a miscibility gap is evident and thus the phase decomposition can also be simulated by the phase-field method.

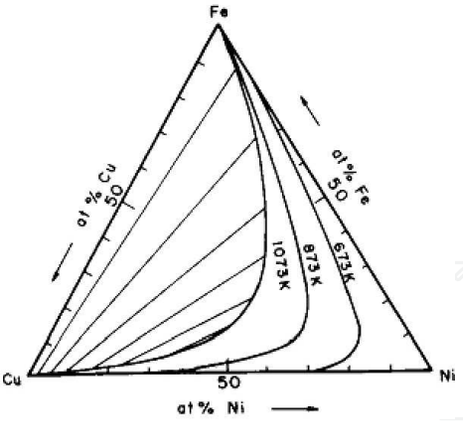

Figure 17. Equilibrium Cu-Ni-Fe phase diagram [16].

The Cahn-Hilliard nonlinear equation for a multicomponent system with a constant mobility can be used for the present simulation, Eq. (7).

The local free energy f_0 was defined using the regular solution model as follows [19]:

$$f_o = f_{Cu}\, c_{Cu} + f_{Ni}\, c_{Ni} + f_{Fe}\, c_{Fe} + \Omega_{Cu-Ni}\, c_{Cu}\, c_{Ni} + \Omega_{Cu-Fe}\, c_{Cu}\, c_{Fe} + \Omega_{Ni-Fe}\, c_{Ni}\, c_{Fe} +$$

$$\Omega_{Cu-Ni-Fe}\, c_{Cu}\, c_{Ni}\, c_{Fe} + RT\,(c_{Cu}\,\ln c_{Cu} + c_{Ni}\ln c_{Ni} + c_{Fe}\ln c_{Fe}) \tag{20}$$

where R is the gas constant, T is the absolute temperature, f_{Cu}, f_{Ni}, and f_{Fe} correspond to the molar free energy of pure Cu, Ni, and Fe, respectively, and $\Omega_{Cu\text{-}Ni}$, $\Omega_{Cu\text{-}Fe}$, $\Omega_{Ni\text{-}Fe}$, and $\Omega_{Cu\text{-}Ni\text{-}Fe}$ represent the interaction parameters. All these thermodynamic constants are shown in **Table 3**.

Parameter	Cu-Ni-Fe alloys	
$\Omega_{Cu\text{-}Ni}$	(9534.49+2.839T) + (−424.255−0.629T)(c_{Cu}-c_{Ni})	
$\Omega_{Cu\text{-}Fe}$	(48206.0 − 8.446T) + (−5918.0 + 5.017T)(c_{Cu}-c_{Fe})	
$\Omega_{Ni\text{-}Fe}$	(−18298.8 + 5.149T) + (14313.6 − 7.659T)(c_{Ni}-c_{Fe})	
$\Omega_{Cu\text{-}Ni\text{-}Fe}$ (J mol^{-1}) [12]	−35982.0 − 12.0T	
f_{Cu}	−8.65T−22.64TlnT−3.13×10^{-3} T^2−7023.9	
f_{Ni}	93.23T−12.54TlnT+1.23×10^{-3} T^2−532.3	
f_{Fe}(J mol^{-1}) [12]	39.0T−26.61TlnT+1.23×10^{-3} T^2−4154.5	
Diffusion coefficient D (cm^2 s^{-1}) [14]	D_{Ni} = 17.0 exp (−279,350 J mol^{-1})/RT	
	D_{Fe} = 6.1 exp (−266,000 J mol^{-1})/RT	
Crystal lattice parameter a (nm) [13]	0.360	
η (nm) [13]	0.0016	
c_{ij} (J m^{-3})	c_{11} = 16.84 × 10^{10}	c_{11}= 24.65 × 10^{10}
Cu/Ni	c_{12}= 12.14×10^{10}	c_{12}= 14.73 × 10^{10}
[15]	c_{44}= 7.54×10^{10}	c_{44} = 12.47 × 10^{10}

Table 3. Values of lattice, diffusion, thermodynamic, and elastic parameters.

The atomic mobility M_i is related to the interdiffusion coefficient $\bar{D}_i$ as follows:

$$\bar{D}_i = M_i\left(\frac{\partial^2 f_0}{\partial c_i^{\,2}}\right) \tag{21}$$

The atomic mobility M_i was determined using Eq. (21) and the procedure proposed by Honjo and Saito [19]:

$$M_{Ni} = \frac{D_{Ni}}{2\Omega_{Cu-Ni} + 4RT} \tag{22}$$

$$M_{Fe} = \frac{D_{Fe}}{2\Omega_{Cu-Fe} + 4RT} \tag{23}$$

http://dx.doi.org/10.5772/64153

where D_{Ni} corresponds to the diffusion coefficient in Cu-50at.%Ni alloy and D_{Fe} to the diffusion coefficient of Fe in Cu. The values of D_{Ni} and D_{Fe} are also indicated in **Table 3**.

The gradient energy coefficient K_i was determined as proposed by Hilliard [4]. It was shown in Eq. (15).

Thus, the gradient energy coefficient K_i was defined as follows:

$$K_{Ni} = \frac{1}{12} a^2 \Omega_{Cu-Ni} \tag{24}$$

$$K_{Fe} = \frac{1}{12} a^2 \Omega_{Cu-Fe} \tag{25}$$

where a represents the lattice parameter also given in **Table 3**.

The effect of coherency elastic-strain energy was introduced into Eq. (7), according to the simple definition proposed by Hilliard [4]. It was shown in Eq. (17).

The elastic constant Y was assumed to be determined with the following equation [4]:

$$Y = \frac{1}{2} c_{11} + 2c_{12} \left(3 - \frac{c_{11} + 2c_{12}}{c_{11} + 2c_{12}(2c_{44} - c_{11} + c_{12})(l^2 m^2 + m^2 n^2 + l^2 n^2)} \right) \tag{26}$$

where l, m, and n are the direction cosines.

The elastic constants, c_{ij} were calculated as follows:

$$c_{ij} = c_{ij}^{Cu-rich} c_{Cu} + c_{ij}^{Ni-rich} (1 - c_{Cu}) \tag{27}$$

Considering the elastic strain energy, f_{el}, Eq. (7) can be rewritten for the c_{Ni} and c_{Fe} as follows:

$$\frac{\partial c_{Ni}(x,t)}{\partial t} = M_{Ni} \nabla^2 \left(\frac{\partial f_o(c)}{\partial c_{Ni}} + \frac{\partial f_{el}}{\partial c_{Ni}} - K_{Ni} \nabla^2 c_{Ni} \right) \tag{28}$$

$$\frac{\partial c_{Fe}(x,t)}{\partial t} = M_{Fe} \nabla^2 \left(\frac{\partial f_o(c)}{\partial c_{Fe}} + \frac{\partial f_{el}}{\partial c_{Fe}} - K_{Fe} \nabla^2 c_{Fe} \right) \tag{29}$$

Equations (28) and (29) were solved numerically using the explicit finite difference method with 101 × 101 points square grid with a mesh size of 0.36 nm and a time-step size up to 10 s. The simulations were performed for the Cu-46at.%Ni-4at.%Fe alloy at temperature of 400°C

for times from 0 to 200 h. This composition was selected for comparison of the morphology and kinetics of the phase decomposition. It is important to mention that the initial composition modulation corresponding to the solution treated sample was calculated using a random-number generator as proposed in reference [19].

Figure 18 shows the calculated concentration profiles of the Cu-46at.%Ni-4at.%Fe alloy aged at 400°C for times from 0 to 200 h. An increase in the amplitude of the composition modulation with aging time can be noticed in both cases. This fact has been associated with the phase decomposition via the spinodal decomposition mechanism [4]. This behavior is also in good agreement with the experimental evidence reported in the literature [18] for the aging of Cu-Ni-Fe alloys. The calculated Cu and Fe concentration profiles are shown in **Figure 19** for the alloys aged at 400°C for 200 h. These plots indicate clearly that the supersaturated solid solution decomposes into two phases: a Cu-Ni-Fe-rich phase with a poor content of Fe and a Ni-Cu-Fe-rich phase with a lower content of Cu and a higher content of Fe. The decomposed Cu-Ni-Fe and Ni-Cu-Fe phases are in agreement with the miscibility gap of the equilibrium Cu-Ni-Fe phase diagram [17].

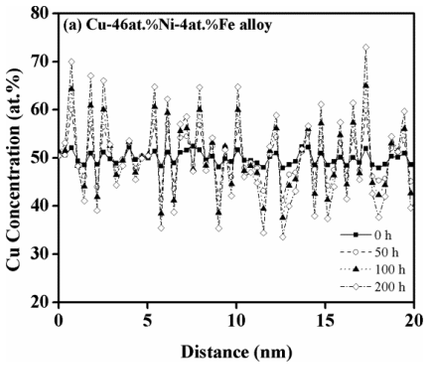

Figure 18. Cu concentration profile of the Cu-46at.%Cu-4at.%Fe alloy aged at 400°C.

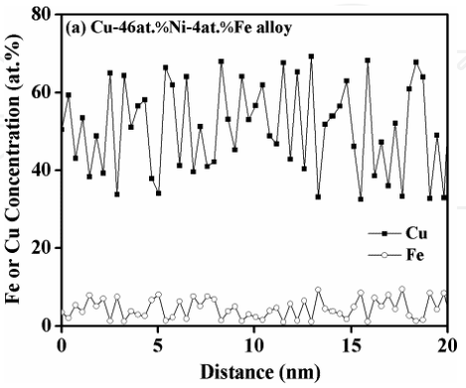

Figure 19. Cu and Fe concentration profile of the Cu-46at.%Cu-4at.%Fe alloy aged at 400°C for 200 h.

The simulated microstructural evolution for the Cu-46at.%Ni-4at.%Fe alloy aged at 400°C for different times is shown in **Figure 20**. The white and black zones correspond to the Ni-Cu-Fe-

http://dx.doi.org/10.5772/64153

rich and Cu-Ni-Fe-rich phases, respectively. The morphology is irregular and interconnected, and it has no preferential alignment in a specific crystallographic direction (**Figure 20(a–c)**). This type of microstructure has been named isotropic [4]. The volume fraction of phases is similar because of the small difference in chemical composition. For higher temperatures, the isotropic morphology at the early stages of aging, as the aging progresses, changes to a cuboid or plate shape, crystallographically aligned along the <100> directions because of the low coherency-strain energy associated with these directions [9].

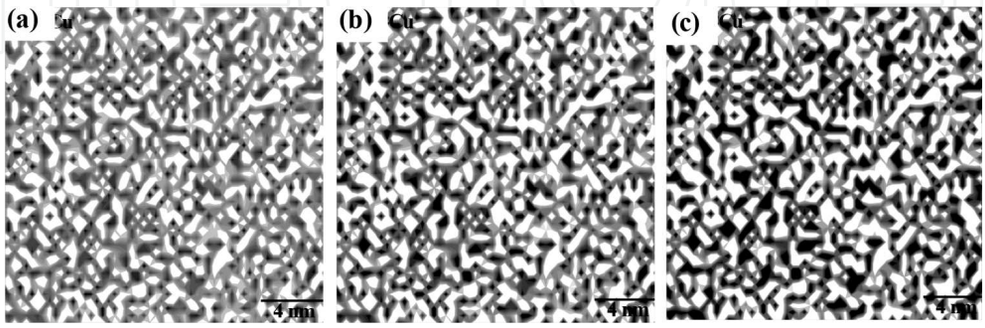

Figure 20. Microstructure evolution of the Cu-46at.%Cu-4at.%Fe alloy aged at 400°C for (a) 50 h, (b) 100 h, and (c) 200 h.

Figure 21 shows the FIM microstructural evolution of the Cu-46at.%Ni-4at.%Fe alloy aged at 400°C for 50 h. FIM image of the solution treated and quenched sample shows the characteristic concentric ring of the (001) plane in both alloys. In the case of the aged samples, brightly imaged zones correspond to the Ni-Cu-Fe-rich phase and dark zones to the Cu-Ni-Fe-rich phase (matrix). The morphology of the decomposed phases was also cuboids or plates aligned in the <100> directions as the aging progressed.

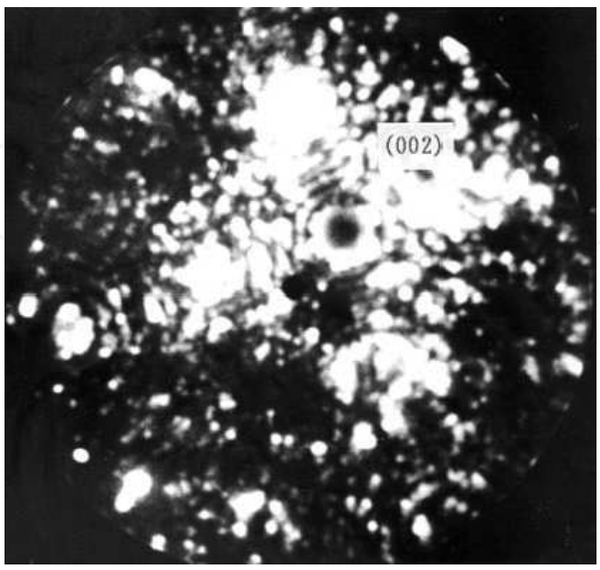

Figure 21. FIM image of the Cu-46at.%Cu-4at.%Fe alloy aged at 400°C for 50 h.

6. Summary

The *phase-field method* for simulation can provide important results, qualitatively and quantitatively, about the microstructural phenomena. This is based on the solution of the Cahn-Hilliard equation and it is a powerful tool to carry out the numerical simulation of the phase decomposition in binary and ternary alloys. The numerical simulation, by mean of the explicit finite difference method, is useful not only to analyze the growth kinetics of phase decomposition but also to determine the morphology of the decomposed phases. Besides, the calculated results show, in general, a good agreement with the experimental results during the aging of these alloys. Additionally, it is interesting to notice that the simulated results enable us to analyze the effect of different parameter such as the atomic mobility and the elastic-strain energy on the growth kinetics and phase morphology of the decomposed phases. Besides, it is important to mention that the numerical simulation permits to analyze the phase decomposition from the early to the late stages of aging which is useful to analyze both the spinodal decomposition and coarsening processes. In the case of the Ni-30at.%Cu alloy, the application of the phase-field method to simulate the microstructural evolution confirmed that the growth kinetics of phase decomposition is very slow in Ni-Cu alloys because of the low atomic diffusive process at temperatures lower than 322°C. However, when a third alloying element, like Fe, is added to this system, the spinodal decomposition process occurs more quickly. Finally, in the case of the Fe-40at.%Cr alloy, it can be clearly observed that the coarsening process of decomposed phases takes place since several concentration fluctuations are grouped in one peak as the aging time progresses.

Acknowledgements

The authors wish to acknowledge financial support from Tecnológico Nacional de México/ Instituto Tecnológico de Pachuca, and SIP-IPN and Conacyt.

Author details

Erika O. Avila-Davila[1], Victor M. Lopez-Hirata[2*] and Maribel L. Saucedo-Muñoz[2]

*Address all correspondence to: vlopezhi@prodigy.net.mx

1 Tecnológic Innstitute of Pachuca, Pachuca de Soto, Hidalgo, Mexico

2 National Polytechnic Institute (ESIQIE), Department of Metallurgy and Materials, Mexico City, Mexico

http://dx.doi.org/10.5772/64153

References

[1] Cahn J.W., Hilliard J.E., Free energy of a nonuniform system I. Interfacial free energy. J. Chem. Phys. 1958; 28, 258–267.

[2] Allen S.M., Cahn J.W., A microscopic theory for antiphase boundary motion and its application to antiphase domain coarsening. Acta Metal. 1979; 27, 1085–1095.

[3] Ginzburg V.L., Landau L.D. On the theory of superconductivity. Zh. Eksp. Teor. Fiz. 1950; 20, 1064–1082.

[4] Hilliard J.E., Phase transformations, ASM, 1970.

[5] Raabe D. Computational materials science, Wiley-VCH, 1998.

[6] Rappaz M., Bellet M., Deville M. Numerical modelling in materials science and engineering, Springer, 1998.

[7] Avila-Davila E.O., Lopez-Hirata V.M., Saucedo-Muñoz M.L., Gonzalez-Velazquez J.L. Microstructural simulation of phase decomposition in Cu-Ni alloys. J. Alloys Comp. 2008; 460, 206–212.

[8] Lifshitz I.M., Slyozov V.V. The kinetics of precipitation from supersaturated solid solution. J. Phys. Chem. Solids. 1961; 19, 35–50.

[9] Kostorz G. Phase transformations in materials, Wiley-VCH, 2001.

[10] Avila-Davila E.O., Lezama-Alvarez S., Saucedo-Muñoz M.L., Lopez-Hirata V.M. Gonzalez-Velazquez J.L., Simulación numérica de la descomposición espinodal en sistemas de aleación hipotéticos A-B y A-B-C. Revista de Metalurgia. 2012; 48, 223–236.

[11] Baker H. Alloy phase diagrams handbook, Vol. 3, ASM International, 1992.

[12] Moser Z., Zakulski W., Spencer P., Hack K. Thermodynamic investigations of solid Cu-Ni and Fe-Ni alloys and calculation of the solid state miscibility gap in the Cu-Fe-Ni system. CALPHAD. 1985; 9, 257–269.

[13] Pearson W.B. A handbook of lattice spacing and structures of metals and alloys, ASM International, 1986.

[14] Mehrer H. Diffusion in solid metals and alloys, Springer-Verlag, 1990.

[15] Dieter G.E. Mechanical metallurgy, Mc Graw Hill, 2001.

[16] Soriano-Vargas O., Avila-Davila E.O., Lopez-Hirata V.M., Dorantes-Rosales H.J., Gonzalez-Velazquez J.L. Spinodal decomposition in an Fe-32 at% Cr alloy during isothermal aging. Mater. Trans. JIM. 2009; 50, 1753–1757.

[17] Lopez-Hirata V.M., Sano N., Sakurai T., Hirano K. A study of phase decomposition in Cu-Ni-Fe alloys. Acta Metall. Mater. 1993; 41, 265–271.

[18] Avila-Davila E.O., Melo-Maximo D.V., Lopez-Hirata V.M., Soriano-Vargas O., Saucedo-Muñoz M.L., Gonzalez-Velazquez J.L. Microstructural simulation in spinodally-decomposed Cu-70 at.%Ni and Cu-46 at.%Ni-4 at.%Fe alloys. Mater. Characterization. 2009; 60, 560–567.

[19] Honjo M., Saito Y. Numerical simulation of phase separation in Fe-Cr binary and Fe-Cr-Mo ternary alloys with use of the Cahn-Hilliard equation. ISIJ Int. 2000; 40, 914–919.

IntechOpen